Supporting Information

Engineering sinter-resistant pyrochlore nanofibers with triple-phase boundaries for acidic oxygen evolution

Yuxin Li,[a†] Mingyu Tang,[a†] Xianbing Miao,[b†] Shiming Zhou[b*] and Yunqian Dai[a*]

[a]School of Chemistry and Chemical Engineering, Southeast University, Nanjing, Jiangsu, 211189, P. R. China

[b]Hefei National Laboratory for Physics Sciences at the Microscale, University of Science and Technology of China, Hefei, Anhui, 230026, P. R. China

[*]Corresponding author: daiy@seu.edu.cn, zhousm@ustc.edu.cn

[†]These three authors contribute equally to this work.

Materials and Methods

Chemical reagents

Polyvinylpyrrolidone (PVP, molecular weight approximately 1.3×10^6), polyacrylonitrile (PAN, molecular weight approximately 1.5×10^5), and ruthenium trichloride ($RuCl_3$, 35–42% content) were supplied by Thermo Fisher Scientific. Turbotriazine(III) nitrate pentahydrate ($Tb(NO_3)_3\cdot5H_2O$) was supplied by Alfa Aesar. N,N-Dimethylformamide (DMF, 99.9% purity), sulfuric acid (H_2SO_4), ethanol, citric acid, and Naphthol were obtained from Sinopharm Chemical Reagent Co., Ltd. All reagents were supplied in their original packaging. Ultrapure water used in all experiments was filtered through a Millerbo filtration system with a resistivity of 18.2 MΩ·cm.

Electrospinning of pyrogranular phase nanofibres

Dissolve 0.375 g of PVP or PAN in 2.18 mL of DMF and stir at 45 °C for 4 hours until a uniform, transparent solution is obtained. Then, add 110 μL of 1 g/mL $Tb(NO_3)_3$ solution and stir for 1 min. Subsequently, add 210 μL of 0.33 g/mL $RuCl_3$ solution and continue stirring for 15 min. Transfer the resulting precursor solution to a 5 mL syringe fitted with a No. 23 metal needle for electrospinning. Under a constant DC voltage, the flow rate was set to 0.3 mL/h, and ambient humidity was maintained below 30%. After electrospinning, the nano-composite nanofiber membrane was transferred to the subsequent calcination step.

Preparation of pyrogranite-phase salt nanoparticles via sol-gel method

Dissolve 0.11 g of $Tb(NO_3)_3$ and 0.07 g of $RuCl_3$ in 10 mL of ultrapure water. Subsequently, add 0.5 g of citric acid. Stir the mixture in an oil bath at 80 °C for 5 h until all water has completely evaporated. Transfer the resulting black powder to a crucible. Perform the first calcination at 600 °C for 6 hours with a heating rate of 5 °C/min. Then conduct a second calcination at 1000 °C for 12 hours, again at a heating rate of 5 °C/min. This yields the pyrogranite-phase salt sample.

OER Performance Testing

Weigh 3.7 mg of the sample into a 5 mL test tube and add 1 mL of ethanol solution.

Subsequently, subject the solution to ultrasonic treatment for 30 minutes. In another 10 mL test tube, weigh a specific amount of carbon powder to prepare a suspension with a concentration of 1 mg/mL. This carbon powder suspension is sonicated until it remains stable at rest without settling. Once a uniform carbon black suspension is obtained, add 750 μL of this suspension to the test tube containing the previously treated catalyst sample and sonicate again for 30 minutes. Subsequently, introduce a small magnetic stir bar, stir the solution overnight, and then sonicate for another 30 minutes. After processing, the stir bar was cleaned by rinsing or ultrasonic treatment and removed. The sample was dried at 50°C for at least 24 h without fan use. Following drying, 1 mL of ethanol and 20 μL of Nafion were added to the test tube, followed by another 30 minutes ultrasonic treatment. After ultrasonication, deposit the ink onto a glassy carbon electrode, allow it to dry for 5–6 hours, and then proceed with testing. This procedure ensures sample uniformity and reaction completeness, providing a reliable foundation for subsequent performance testing. Assemble the prepared glassy carbon electrode with a carbon rod counter electrode and a Hg_2Cl_2/KCl reference electrode to form a three-electrode system for evaluating its water electrolysis performance.

EIS measurements were performed over a frequency range from 0.01 to 100000Hz with an AC amplitude of 5 mV.

The relative electrochemical surface area (ECSA) of the catalyst was estimated using the double-layer capacitance (C_{dl}) method. Cyclic voltammetry curves were measured at different scan rates (20, 40, 60, 80, and 100 $mV \cdot s^{-1}$) in the non-Faradaic potential range, and C_{dl} values were obtained by linearly fitting the current differences to the scan rate. ECSA was calculated using the formula $ECSA=C_{dl}/C_s$, where the standard specific capacitance Cs[1] was set to 35 $\mu F \cdot cm^{-2}$.

To ensure data comparability, all potentials are converted to values relative to the reversible hydrogen electrode (RHE), where $E_{RHE}=E_{SCE} + 0.2415 + 0.0591 \times pH$. The overpotential ($\eta$) for the oxygen evolution reaction (OER) is calculated as: $\eta=E_{RHE} - 1.23$.

The AST test conditions involve cycling 10,000 revolutions at a scan rate of 0.5 V/s within a voltage range of 1.2–1.6 V vs. RHE.

Contact Angle Measurement

Following the compaction of powder into pellets or its deposition onto electrodes, the contact angle of the sample powder is measured using a contact angle micrometer. Bubbles formed during the water electrolysis experiment are captured by the high-speed camera of the contact angle micrometer.

Characterisation

TEM images were acquired using a FEI Tecnai G220 microscope at 200 kV. X-ray diffraction (XRD) analysis was performed at room temperature using an Ultima IV instrument with a continuous scan rate of 5°/min under a focused beam configuration employing Cu-Kα radiation (wavelength 1.54 Å). Scanning electron microscopy (SEM) images were obtained using a field emission scanning electron microscope (FEI, Inspect F50). X-ray photoelectron spectroscopy (XPS) measurements were performed with a Thermo-VG Scientific Esea Lab 250.

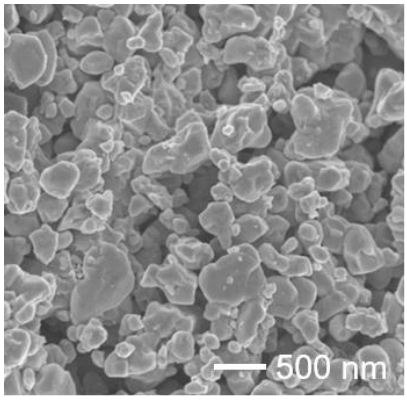

Fig. S1 Representative SEM image showing the aggregated particulate morphology obtained via the conventional sol-gel synthesis route.

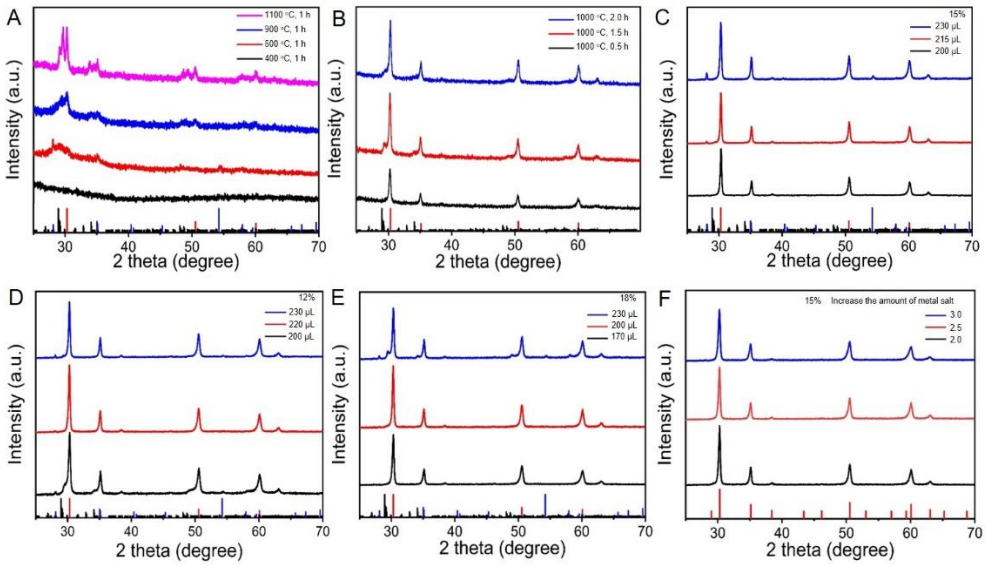

Fig. S2 XRD analysis of phase evolution during $Tb_2Ru_2O_7$ nanofiber synthesis. (A) Patterns of nanofibers (15 wt% polymer) calcined at different temperatures. (B) Patterns of nanofibers (15 wt% polymer) calcined at a fixed temperature for different durations. (C-E) Patterns of nanofibers prepared with different polymer concentrations (12, 15, 18 wt%) and varying metal salt precursor loadings. (F) Patterns of nanofibers (15 wt% polymer) prepared with increased (multi-fold) metal salt precursor content. All patterns demonstrate the formation of the phase-pure pyrochlore structure under the investigated synthesis conditions. The red vertical line corresponds to the standard card JCPDS No. 28-1288 for $Tb_2Ru_2O_7$. The black vertical line corresponds to the standard card JCPDS No. 39-1026 for Tb_3RuO_7. The blue vertical line corresponds to the standard card JCPDS No. 28-1139 for RuO_2.

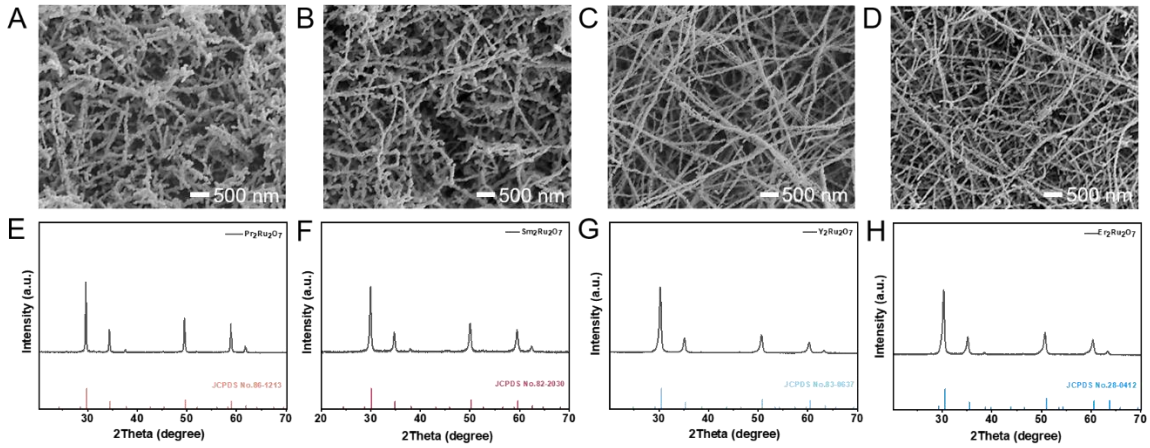

Fig. S3 Representative SEM images of calcined nanofibers with different A-site cations of (A) $Pr_2Ru_2O_7$, (B) $Sm_2Ru_2O_7$, (C) $Y_2Ru_2O_7$, and (D) $Er_2Ru_2O_7$. Corresponding XRD patterns of (E) $Pr_2Ru_2O_7$, (F) $Sm_2Ru_2O_7$, (G) $Y_2Ru_2O_7$, and (H) $Er_2Ru_2O_7$. These four compounds correspond to the standard cards $Pr_2Ru_2O_7$ (JCPDS No. 86-1213), $Sm_2Ru_2O_7$ (JCPDS No. 82-2030), $Y_2Ru_2O_7$ (JCPDS No. 83-0637), and $Er_2Ru_2O_7$ (JCPDS No. 28-0412).

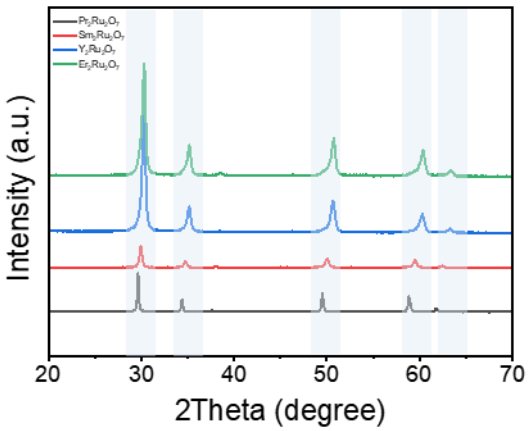

Fig. S4 XRD patterns of the $A_2Ru_2O_7$ (A = Pr, Sm, Y, Er) pyrochlore nanofiber series. Patterns are vertically offset for clarity.

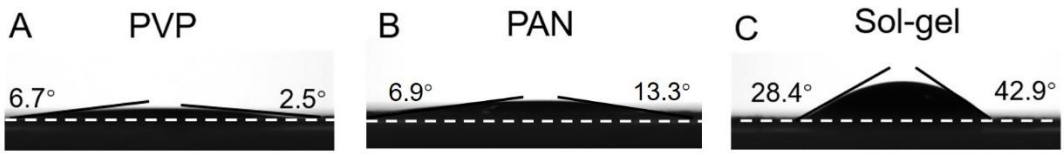

Fig. S5 Water contact angles measured on (A) PVP-derived and (B) PAN-derived $Tb_2Ru_2O_7$ nanofibers, along with (C) sol-gel synthesized nanoparticles for comparison.

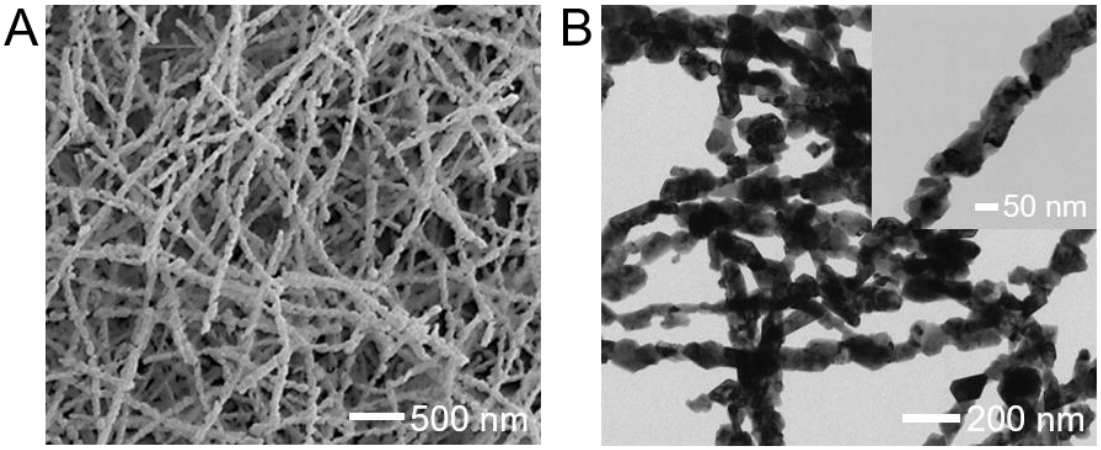

Fig. S6 Morphological characterization of PVP-derived $Tb_2Ru_2O_7$ nanofibers. (A) SEM image. (B) TEM image, inset shows higher-magnification view of individual nanofiber.

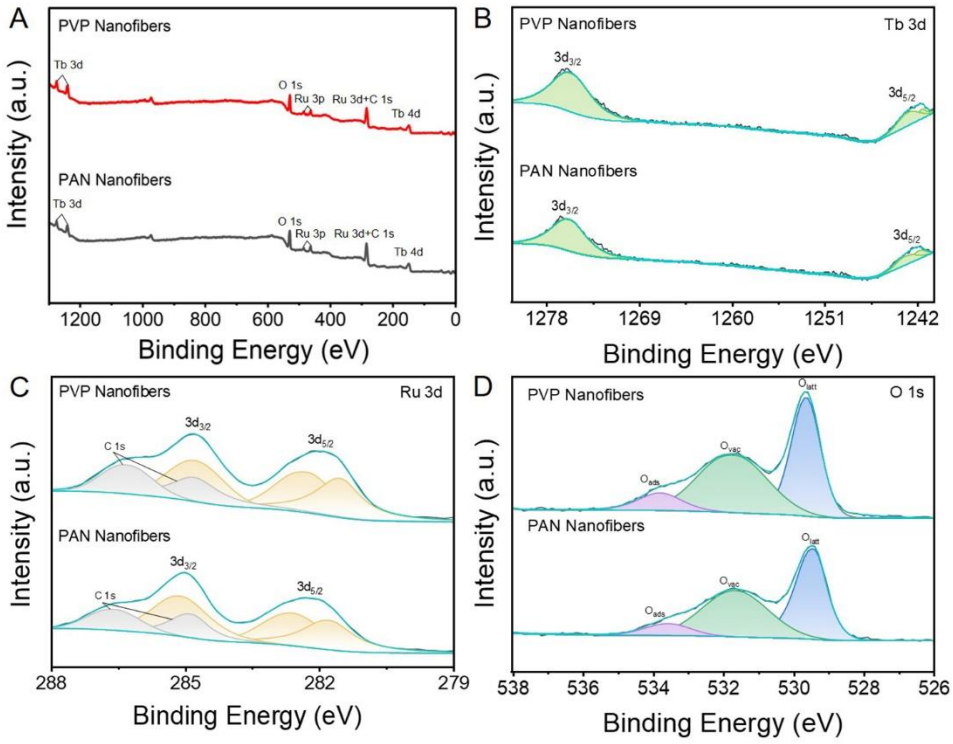

Fig. S7 XPS spectra of PVP-derived and PAN-derived nanofibers: (A) survey, (B) Tb 3d, (C) Ru 3d, and (D) O 1s high-resolution scans. XPS analysis reveals that in both PVP- and PAN-derived nanofibers, Tb exists stably in the +3 oxidation state, while Ru exhibits a mixed valence state of Ru^{3+} and Ru^{4+}, confirming that the electronic modulation effect of the pyrochlore framework effectively suppresses excessive oxidation of Ru. The primary difference between the two catalysts lies in the chemical state of oxygen, reflected in their distinct oxygen vacancy contents.

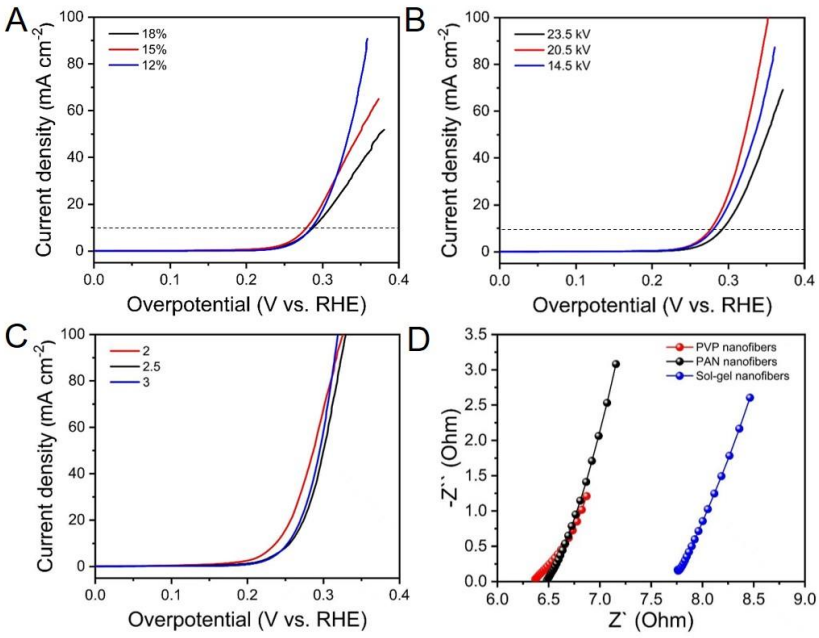

Fig. S8 Electrochemical OER performance of $Tb_2Ru_2O_7$ catalysts. (A) Polarization curves of electrospun nanofibers prepared with different polymer concentrations. (B) Polarization curves of electrospun nanofibers prepared with a fixed polymer concentration (15 wt%) under different applied voltages. (C) Polarization curves of nanofibers (15 wt% polymer) prepared with increased metal salt precursor loading. (D) Nyquist plots from electrochemical impedance spectroscopy measured at open circuit potential.

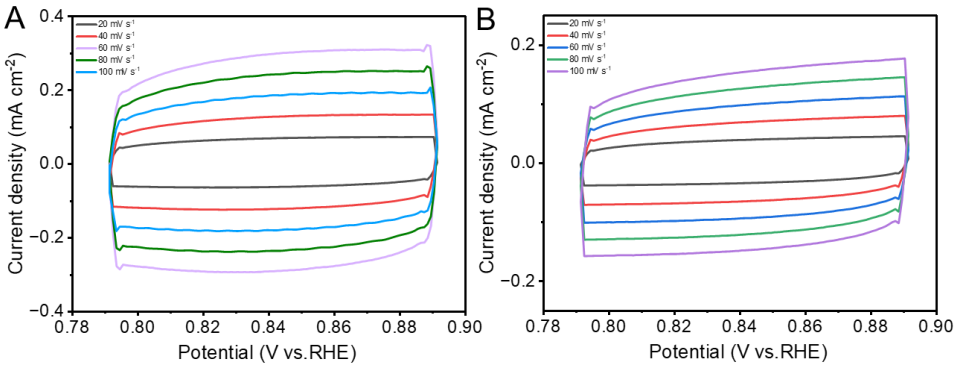

Fig. S9 CV curves of (A) PVP-derived and (B) PAN-derived $Tb_2Ru_2O_7$ nanofibers under different scan rates in 0.5 M H_2SO_4.

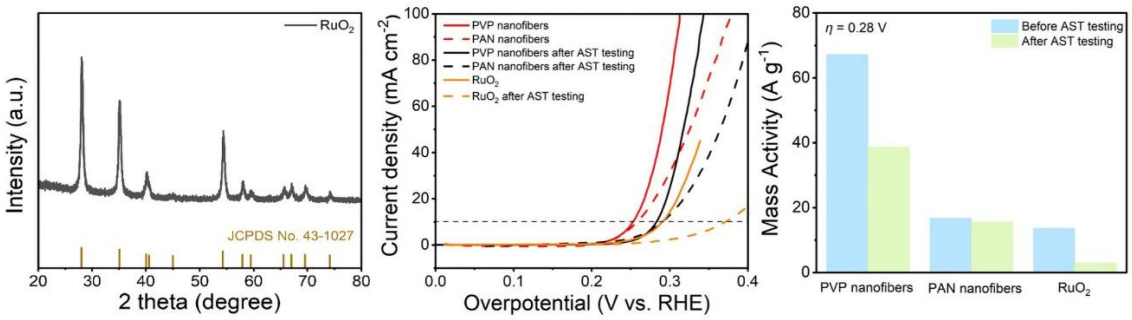

Fig. S10 (A) XRD patterns of the RuO_2. Comparison of electrochemical performance among three catalysts before and after accelerated stress testing (AST) for 10000 cycles: (B) LSV curves; (C) Mass activity histogram at an overpotential of 0.28 V. All polarization curves were recorded in O_2-saturated 0.5 M H_2SO_4 with a scan rate of 20 $mV \cdot s^{-1}$.

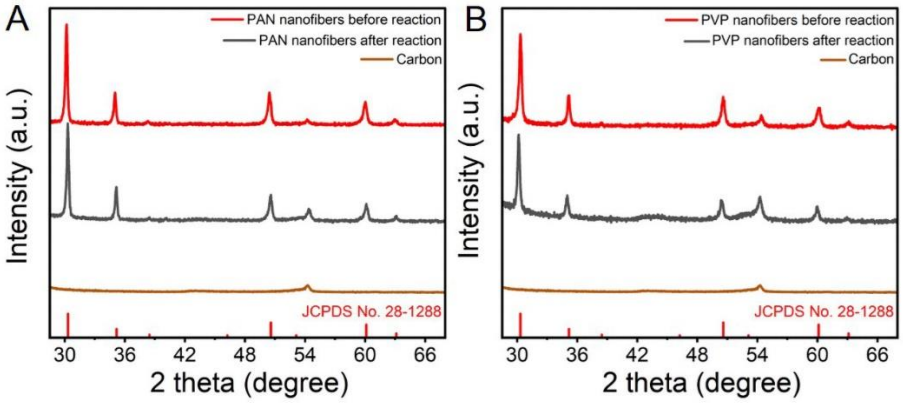

Fig. S11 XRD patterns before and after electrochemical reaction: (A) PVP-derived and (B) PAN-derived nanofibers.

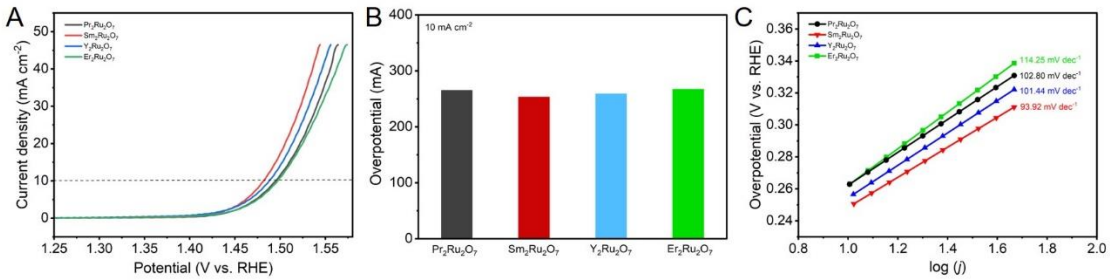

Fig. S12 Electrochemical OER performance of $A_2Ru_2O_7$ (A=Pr, Sm, Y, Er). (A) Polarization curves of electrospun nanofibers prepared with different polymer concentrations. (B) Overpotential at a current density of 10 mA cm^{-2}. (C) Tafel slope. All polarization curves were recorded in O_2-saturated 0.5 M H_2SO_4 with a scan rate of 20 mV·s^{-1}.

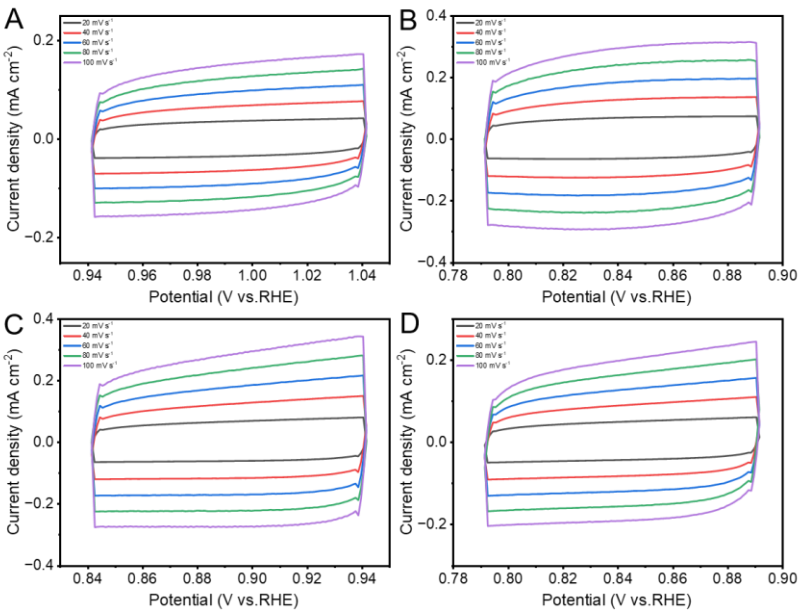

Fig. S13 CV curves of (A) $Pr_2Ru_2O_7$, (B) $Sm_2Ru_2O_7$, (C) $Y_2Ru_2O_7$ and (D) $Er_2Ru_2O_7$, nanofibers under different scan rates in 0.5 M H_2SO_4.

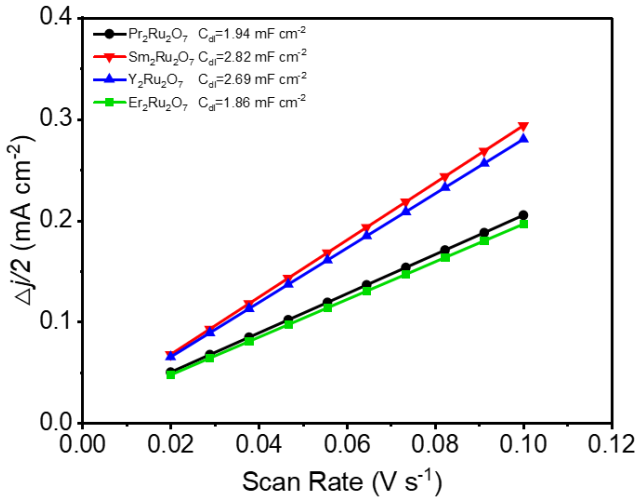

Fig. S14 The double-layer capacitances derived from the CV curves at various scan rates of $A_2Ru_2O_7$（A=Pr, Sm, Y, Er).

Table S1 Refined parameters for $Tb_2Ru_2O_7$.

$Tb_2Ru_2O_7$	x	y	z	U_{iso}
Tb	0.50000	0.50000	0.50000	0.05673
Ru	0.00000	0.00000	0.00000	0.00238
O1	0.33530	0.12500	0.12500	0.07154
O2	0.37500	0.37500	0.37500	0.18077
a=b=c=10.209 Å, α=β=γ=90°, space group $Fd\bar{3}m$				

Table S2 The LSV test compared with other reported literature

Catalyst	Stability (h)	Reference
Pt-RuO_2	215 mV	[2]
$Sr_{1-\delta}IrMnO_x$	221 mV	[3]
W-$NiCo_2O_4$	289 mV	[4]
Co_3O_4/Ni-RuO_2/rGO	195 mV	[5]
IrO_2/IrTaOx	211 mV	[6]
Mo-Co_3O_4	310 mV	[7]
H-Ir@Co_3O_4	248 mV	[8]
$Ir_{CAEN-1000-6}$	250 mV	[9]
$Y_{1.75}Co_{0.25}Ru_2O_{7-\delta}$	275 mV	[10]
$Tb_2Ru_2O_7$	246 mV	This work

1. R. Ram, L. Xia, H. Benzidi, A. Guha, V. Golovanova, A. Garzón Manjón, D. Llorens Rauret, P. Sanz Berman, M. Dimitropoulos, B. Mundet, E. Pastor, V. Celorrio, C. A. Mesa, A. M. Das, A. Pinilla-Sánchez, S. Giménez, J. Arbiol, N. López, F. P. García de Arquer, *Science*, 2024, **384**, 1373-1380.
2. X. Cao, L. Miao, W. Jia, H. Qin, G. Lin, R. Ma, T. Jin, L. Jiao, *Nat. Commun.*, 2025, **16**, 6217.
3. J. W. Zhao, K. Yue, Z. Pei, J. Yang, D. Luan, X. W. Lou, *Adv. Mater.*, 2025, **37**, e15749.
4. S. Li, S. Zhao, S.F. Hung, L. Deng, L. Wang, F. Shi, A. Dong, Y. Zhang, T.Y. Chen, F. Hu, L. Li, S. Ramakrishna, Y. Wu, S. Peng, *J. Am. Chem. Soc.*, 2025, **147**, 33770-33779.
5. W. Yang, Z. Wang, J. Zhang, L. Jia, J. Li, X. Chen, X. Liu, H. Zhang, J. Lin, M. Zhao, Q. Chen, *Angew. Chem. Int. Ed.*, 2025, **64**, e202509768.
6. Q. Guo, R. Li, Y. Zhang, Q. Zhang, Y. He, Z. Li, W. Liu, X. Liu, Z. Lu, *Nano-Micro Letters*, 2025, **17**, 165.
7. Z. Liu, W. Shen, X. Liang, J. Liang, K. Xu, X. Ge, J. Lu, H. Liu, J. Xiao, L. Wang, J. Gao, J. Liu, *ACS Catal.*, 2025, **15**, 8943-8953.
8. Y. Wang, Y. Qin, S. Liu, Y. Zhao, L. Liu, D. Zhang, S. Zhao, J. Liu, J. Wang, Y. Liu, H. Wu, B. Jia, X. Qu, H. Li, M. Qin, *J. Am. Chem. Soc.*, 2025, **147**, 13345-13355.
9. S. Zhang, B. Ji, K. Ding, Y. Yang, Y. Zheng, Y. Tang, *Adv. Energy Mater.*, 2025, **15**, e03229.
10. N. Han, S. Feng, Y. Liang, J. Wang, W. Zhang, X. Guo, Q. Ma, Q. Liu, W. Guo, Z. Zhou, S. Xie, K. Wan, Y. Jiang, A. Vlad, Y. Guo, E. M. Gaigneaux, C. Zhang, J. Fransaer, X. Zhang, *Adv. Funct. Mater.*, 2023, **33**, 2208399.